Strong coupling between two-dimensional transition metal dichalcogenides and plasmonic-optical hybrid resonators

Ying Liu,[1,2,*] Zebin Zhu,[1,2,*] Jisong Qian,[1,2] Jing Yuan,[1,2] Jiaxu Yan,[3] Ze Xiang Shen,[4,†] and Liyong Jiang[1,2,‡]

[1]*Institute of Micro-nano Photonics and Quantum Manipulation, School of Science, Nanjing University of Science and Technology, Nanjing 210094, China*

[2]*MIIT Key Laboratory of Semiconductor Microstructure and Quantum Sensing, Nanjing University of Science and Technology, Nanjing 210094, China*

[3]*Key Laboratory of Flexible Electronics (KLOFE) and Institute of Advanced Materials (IAM), Jiangsu National Synergistic Innovation Center for Advanced Materials (SICAM), Nanjing Tech University, Nanjing 211816, China*

[4]*Centre for Disruptive Photonic Technologies, School of Physical and Mathematical Sciences, Nanyang Technological University, Singapore 637371, Singapore*

(Received 2 July 2021; revised 11 October 2021; accepted 27 October 2021; published 15 November 2021)

In the past decade, strong coupling of two-dimensional transition metal dichalcogenides (TMDs) with plasmonic and optical resonators has become an attractive field in cavity quantum electrodynamics. On one hand, how to enhance the Rabi splitting in such a system is important for applications. On the other hand, the underlying strong-coupling mechanism is not clear yet, especially for the complicated coupling case related to multiple photonic quasiparticles. Here we propose a plasmonic-optical hybrid resonator composed of a Au nanoantenna and photonic crystal cavity. When monolayer MoS_2 is coupled with this hybrid resonator, we demonstrate a large Rabi splitting up to 460 meV, which is better than ever reported in similar systems. More importantly, we provide a deeper understanding of complicated coupling mechanisms in such a hybrid system, paving the way for studying strong light–matter interactions with multiple photonic quasiparticles in TMD materials coupled with different plasmonic-optical hybrid resonators.

DOI: 10.1103/PhysRevB.104.205118

Introduction. Strong coupling is a hot spot in cavity quantum electrodynamics (QED). Based on the strong light–matter interactions, we can observe many interesting physical phenomena, such as Bose-Einstein condensation, vacuum Rabi splitting, optical Stark effect, and long-range energy transfer [1–5]. In recent years, Rabi splitting has been extensively studied in dye molecules, quantum dots, and two-dimensional (2D) semiconductor materials coupled with nanoscale plasmonic resonators, which simultaneously show strong localization and low mode volume [6–12]. In particular, 2D transition metal dichalcogenides (TMDs) have become the most ideal active materials in cavity QED study due to their high transition dipole moment and large binding energy [13–18]. For example, Qin *et al.* reported strong plasmon-exciton coupling in monolayer WS_2 coupled with a gap-plasmon resonator and demonstrated that the effective exciton number contributing to the coupling could be reduced down to the single-digit level [10]. Shan *et al.* reported a Au grating/MoS_2/Al_2O_3/Au/Si sandwiched heterostructure, based on which the ultrafast plasmonic hot electron transfer could be directly observed under the strong-coupling conditions [19]. These studies indicate that 2D TMD materials coupled with plasmonic resonators show great application potential in ultrafast optical switching, optoelectronic devices, and quantum information processing [20–25].

Except for the plasmon-exciton, the photon-exciton and magnetic dipole-exciton interactions have also been investigated in 2D TMD materials coupled with optical resonators, such as Fabry-Perot (FP) cavities, photonic crystal (PC) cavities, and whispering-gallery-mode (WGM) resonators [26–32]. As compared to plasmonic resonators, the mode volume V of optical resonators is usually not small enough to provide a large coupling strength g since $g \propto \sqrt{N/V}$ [10], where N is the exciton number contributing to the coupling process. However, the quality factor Q of optical resonators is usually much higher than plasmonic resonators due to lower loss in the dielectric materials. This advantage of optical resonators is quite useful to improve the rate of spontaneous emission of excitons in TMD materials [33]. In particular, the 2D PC cavity can not only provide a high-quality factor Q, but also be easily integrated with the 2D semiconductor materials [28].

When 2D TMD materials are coupled with plasmonic-optical hybrid resonators, the coupling process will be much more complicated than the case of 2D TMDs coupled with pure plasmonic or optical resonators [26,34–37]. Recent research indicates that the Rabi splitting can be further enhanced in 2D TMDs coupled with a plasmonic-optical hybrid resonator [38]. Unfortunately, the complicated coupling mechanism is not clear yet among different photonic quasiparticles, which will significantly influence the understanding, design, and application of strong-coupling phenomena of 2D

*These authors contributed equally to this work.
†zexiang@ntu.edu.sg
‡Corresponding author: jly@njust.edu.cn

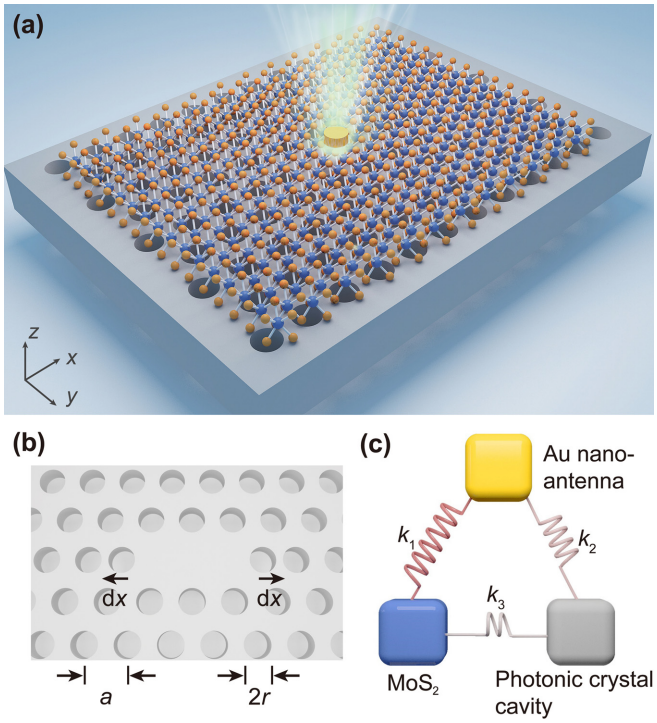

FIG. 1. (a) Schematic of monolayer MoS_2 coupled with a Au NA-PC cavity hybrid resonator. (b) Schematic of the 2D PC cavity. (c) Oscillator model of the hybrid system.

TMD materials coupled with plasmonic-optical hybrid resonators. In this paper we will study the strong light–matter interactions in 2D TMD material coupled with a plasmonic-optical hybrid resonator. We will demonstrate enhanced Rabi splitting in such a hybrid system and clearly reveal the underlying mechanism among multiple photonic quasiparticles.

Results. As shown in Fig. 1(a), the hybrid resonator is constructed by a typical Au nanoantenna (NA) and a typical 2D PC cavity. Monolayer molybdenum disulphide (MoS_2) is placed on the top of a 160-nm-thick 2D PC cavity, and then a 30-nm-thick Au disk is placed on the surface of MoS_2. The 2D PC cavity is made of triangular-lattice arranged air holes on the Si_3N_4 membrane ($n = 2.03$), and two air holes in the center are removed to construct an L_2-type line defect [Fig. 1(b)]. The lattice constant a = 350 nm and the hole radius $r = 0.32$a. In order to improve the quality factor of the cavity, two air holes near the line defect are moved outward with a distance of $dx = 0.2$a [39,40]. The relative dielectric constant of Au is determined by the experimental results of Johnson and Christy [41]. The dielectric properties of excitons in monolayer MoS_2 are described by the classical Lorentz model [42],

$$\varepsilon = \varepsilon_\infty + \frac{f_x \omega_0^2}{\omega_0^2 - \omega^2 - i\Gamma\omega}, \tag{1}$$

where $\varepsilon_\infty = 1$ is the permittivity of the background, f_x is the oscillator strength, ω_0 is the resonant frequency of excitons, and Γ is the linewidth. In order to clearly reveal the coupling mechanism between excitons and other photonic quasiparticles, here we only consider one main exciton peak located at 663 nm for monolayer MoS_2.

Figure 1(c) shows the corresponding oscillator model of the hybrid system. We use k_1, k_2, and k_3 to represent the interaction coefficients of Au NA-MoS_2, Au NA-PC cavity, and PC cavity-MoS_2, respectively. Generally, k_1 is much larger than k_2 and k_3. We investigate the coupling process of multiple photonic quasiparticles in this hybrid system by simultaneously conducting the numerical analysis based on the quantum coupling model and the numerical simulation based on the finite difference time domain (FDTD) numerical simulation method. In our simulation, the monolayer MoS_2 is introduced as a 1-nm-thick layer with the provided permittivity [43,44]. A Gaussian source polarized along the y direction with a waist radius of 1 μm is used to excite the coupled oscillations. For x, y, and z directions, the boundary conditions are set to perfectly matched layer (PML). The mesh size is set as 0.6 nm near the Au NA and PC cavity for x, y, and z directions, and 0.25 nm for z direction in the MoS_2 layer.

For the purpose of comparison, we have firstly investigated the coupling between Au NA and monolayer MoS_2 on a pure Si_3N_4 substrate without a PC cavity. As shown in Fig. 2(a), the total absorption spectrum of the system splits into three branches and presents obvious anticrossing behavior with the change of the Au disk's radius r_{Au}. As f_x increases, the splitting of three branches becomes larger and larger [Fig. 2(b)], which implies that the interior coupling strength g also gradually increases because $g \propto \sqrt{f_x}$ [45]. Figure 2(c) compares the absorption spectra of Au NA, monolayer MoS_2, and their composite structure. The pure Au NA with $r_{Au} =$ 40 nm shows an absorption peak at $\lambda = 667$ nm due to the localized surface plasmon (LSP) effect, and the monolayer MoS_2 shows a main absorption peak of exciton (Ex) at λ = 663 nm when $f_x = 0.3$ and a typical absorption peak of epsilon-near-zero (ENZ) mode at $\lambda = 581$ nm. Actually, the total absorption spectrum of the composite structure is the coupling result of three photonic quasiparticles, i.e., LSP, Ex, and ENZ mode. This conclusion can be further demonstrated based on the corresponding electric field distribution of three absorption peaks of the composite structure. As shown in Fig. 2(d), the absorption peaks at $\lambda = 684$ nm (branch 1) and $\lambda = 650$ nm (branch 2) exhibit a typical electric field distribution of LSP, while the absorption peak at $\lambda = 567$ nm (branch 3) presents a typical electric field distribution of an ENZ mode, since the energy is mainly localized inside the monolayer MoS_2 (see inset).

The LSP-Ex-ENZ coupling process can be described by the Hamiltonian equation of a quantized coupling system

$$\hat{\boldsymbol{H}}|s\rangle = E_s|s\rangle, \tag{2}$$

where $\hat{\boldsymbol{H}}$ is the Hamiltonian operator which can be written as [32]

$$\hat{\boldsymbol{H}} = \begin{pmatrix} E_{\mathrm{LSP}} + i\hbar\Gamma_{\mathrm{LSP}}/2 & g_{\mathrm{LSP,Ex}} & g_{\mathrm{LSP,ENZ}} \\ g_{\mathrm{LSP,Ex}} & E_{\mathrm{Ex}} + i\hbar\Gamma_{\mathrm{Ex}}/2 & g_{\mathrm{Ex,ENZ}} \\ g_{\mathrm{LSP,ENZ}} & g_{\mathrm{Ex,ENZ}} & E_{\mathrm{ENZ}} + i\hbar\Gamma_{\mathrm{ENZ}}/2 \end{pmatrix}. \tag{3}$$

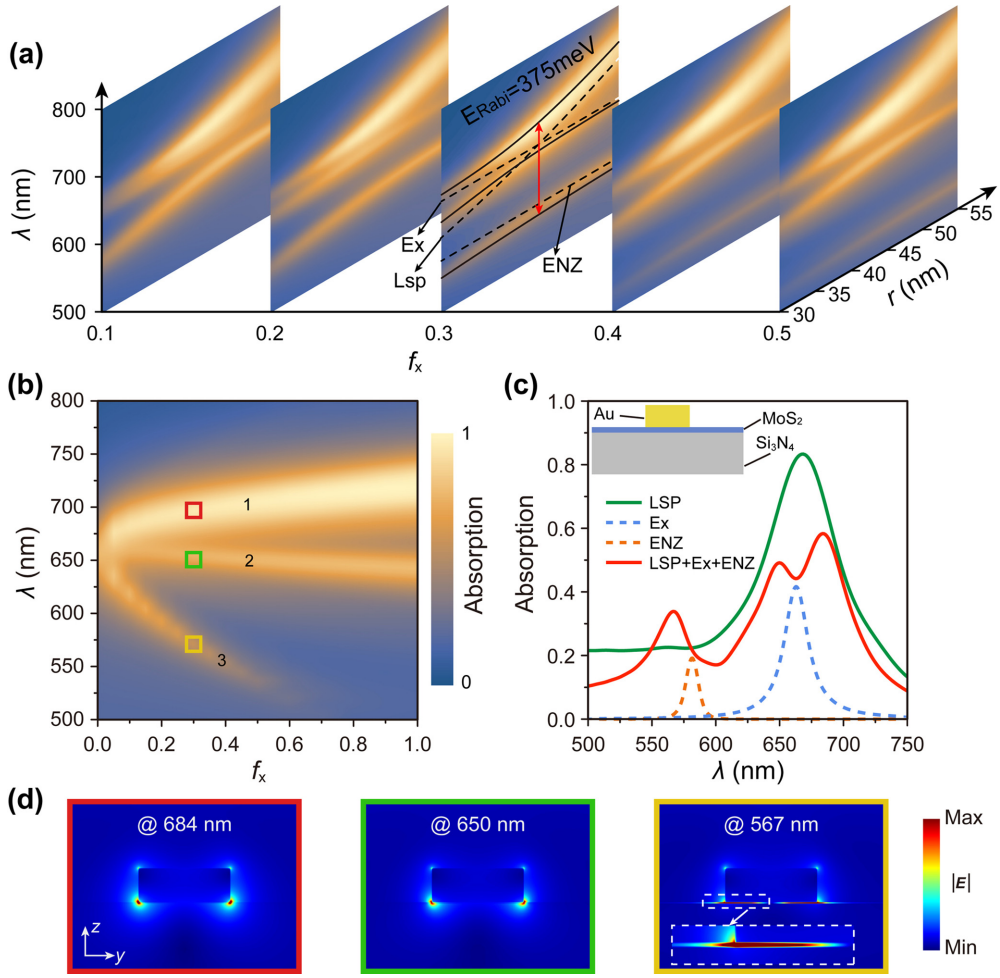

FIG. 2. (a) Absorption spectrum of monolayer MoS_2 coupled with Au NAs. The solid black line is the anticrossing curve fitted by the coupled oscillator model. (b) Absorption spectrum as a function of f_x when $r_{Au} = 40$ nm. Red, green, and yellow squares correspond to three absorption peaks when $f_x = 0.3$. (c) Absorption curves of LSP mode, Ex mode, ENZ mode, and their coupled mode when $r_{Au} = 40$ nm. The inset shows the schematic of the coupled structure. (d) Electric field distributions on the y-z plane for three absorption peaks in (b).

$|s\rangle$ $(s = 1, 2, 3)$ stands for the probability wave function of the linewidth of the three modes contributing to each branch and meets the normalization condition $\langle s|s\rangle = 1$. E_s is the energy of each branch. Based on Eqs. (2) and (3), we got the fitted curves as represented by the solid black lines in Fig. 2(a) when $f_x = 0.3$. In particular, when $r_{Au} = 40$ nm, the Rabi splitting reaches 375 meV, and the $g_{LSP,Ex}$, $g_{LSP,ENZ}$, and $g_{Ex,ENZ}$ are fitted to be 57 meV, 137 meV, and 0.14 meV, respectively.

Let us explain the formation mechanisms of three branches. Branches 1 and 2 are mainly caused by the Mie resonance. For a single Au disk ($r_{Au} = 40$ nm), the absorption peak of the Mie resonance is located at 667 nm and the corresponding ε_{Au} is $-14.2 + 1.47i$. When Au disk and monolayer MoS_2 form a composite structure, its equivalent dielectric constant ε_{eff} can be written as [46]

$$\varepsilon_{eff} = \varepsilon_{Au} + \left(\varepsilon_{MoS_2} - 1\right)\frac{d_{MoS_2}}{d_{Au,eff}}, \tag{4}$$

where d_{MoS_2} is the thickness of monolayer MoS_2 with a typical value of 1 nm. $d_{Au,eff}$ is the equivalent thickness of interaction between Au and MoS_2. In particular, when $d_{Au,eff} = 6.2$ nm, the $\mathrm{Re}(\varepsilon_{eff})$ and $\mathrm{Im}(\varepsilon_{eff})$ as a function of f_x are plotted in Figs. 3(a) and 3(b), respectively. The composite structure satisfies $\varepsilon_{eff} = -14.2 + 1.47i$ at about 650 nm and 684 nm, which can well explain the formation mechanism of branches 1 and 2 in Fig. 2.

Branch 3 is related to the ENZ mode. From Fig. 3(c) we can see two points of $\mathrm{Re}(\varepsilon_{MoS_2}) = 0$ located at 581 nm and 663 nm respectively, while only one point of $\mathrm{Im}(\varepsilon_{MoS_2}) = 0$ is located at 581 nm. According to the continuity condition of the normal electric displacement vector at the metal-medium interface, i.e., $D_{MoS_2,\perp}$–$D_{Au,\perp} = \sigma_f$, where σ_f is the surface density of free charge on the interface between the Au disk and monolayer MoS_2, we can get [47]

$$E_{MoS_2,\perp} = \frac{\varepsilon_{Au}E_{Au,\perp} + \sigma_f}{\varepsilon_{MoS_2}}. \tag{5}$$

On the basis of Eq. (5), at the two zero points of $\mathrm{Re}(\varepsilon_{MoS_2})$, electric field magnitudes inside the monolayer MoS_2 should both be significantly larger than that inside the adjacent

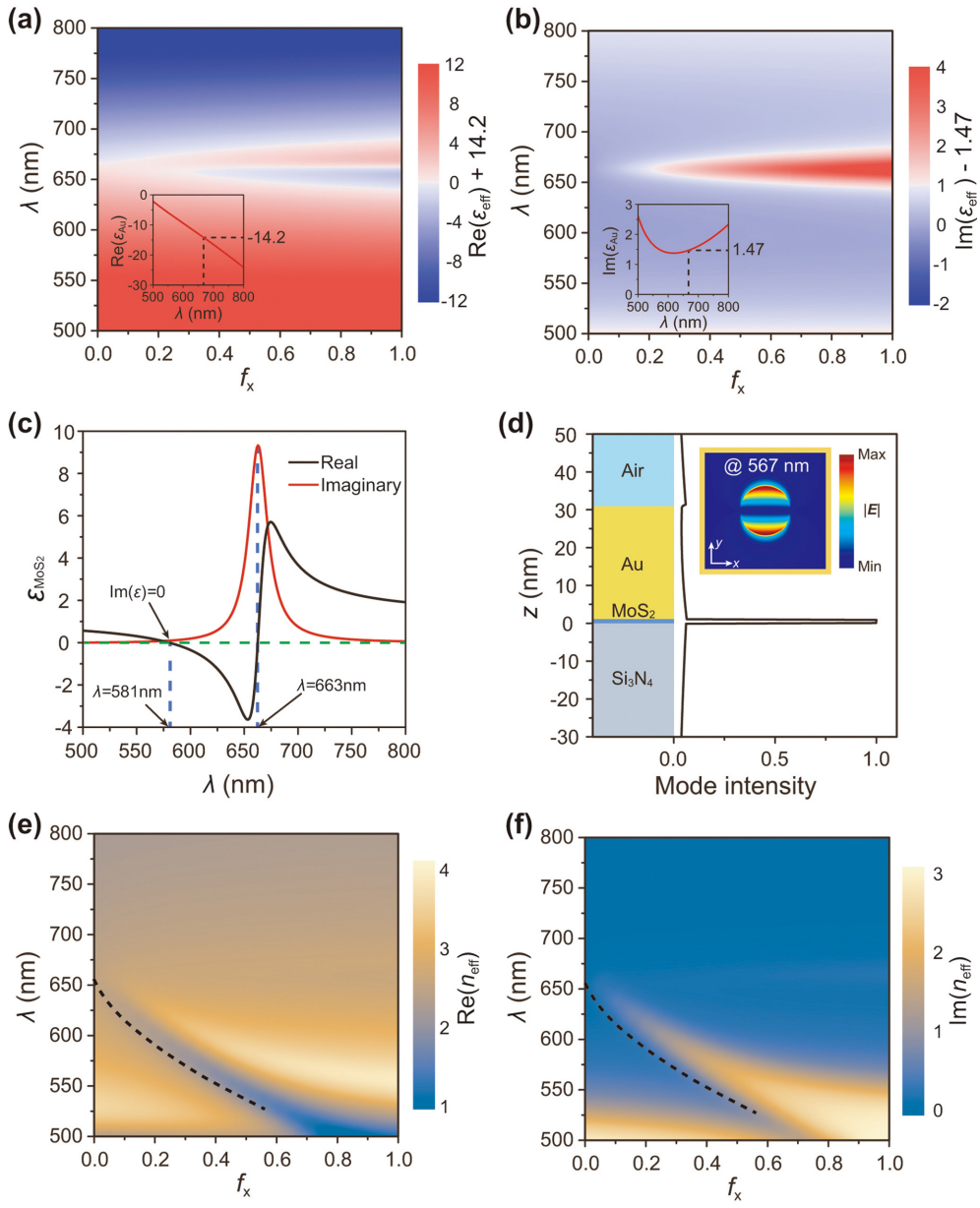

FIG. 3. (a) Re(ε_{eff}) and (b) Im(ε_{eff}) as a function of f_x. The insets in (a) and (b) show the Re(ε_{Au}) and Im(ε_{Au}), respectively. (c) ε_{MoS_2} as a function of wavelength when $f_x = 0.3$. (d) A mode intensity distribution of the ENZ mode at 567 nm along the z direction. The inset shows the electric filed distribution in the center of the MoS_2 layer. (e), (f) Re(n_{eff}) and Im(n_{eff}) of the ENZ mode as a function of f_x.

materials. However, we can only see the ENZ mode near 581 nm because both Re(ε_{MoS_2}) and Im(ε_{MoS_2}) should be zero according to the complex form of refractive index $n = [\text{Re}(\varepsilon_{MoS_2}) + \text{Im}(\varepsilon_{MoS_2})i]^{1/2}$. As shown in Fig. 3(d), it can be observed that the electric field of the ENZ mode is mainly concentrated in the MoS_2 layer (see inset). Figures 3(e) and 3(f) show the Re(n_{eff}) and Im(n_{eff}) of the ENZ mode as a function of λ and f_x, from which we can find that the valley value of Re(n_{eff}) and the peak value of Im(n_{eff}) are consistent with branch 3 in Fig. 2(b) in trend. Since the frequency of an ENZ mode is determined by ε_{MoS_2}, which can be influenced by the surface density of free charge rather than bounded charge on the Au disk-MoS_2 interface, the coupling strength $g_{\text{LSP,ENZ}}$ is much higher than $g_{\text{Ex,ENZ}}$.

Then we have studied the coupling between Au NA and the PC cavity, as well as the coupling between the PC cavity and monolayer MoS_2. The former case shows a Fano-like weak coupling [45,48–51], while the latter case shows almost no coupling. More results and discussion are available in the Supplemental Material [52].

Finally, we have investigated the coupling between monolayer MoS_2 and the Au NA-PC cavity hybrid resonator. As shown in Figs. 4(a) and 4(b), the absorption spectrum of the coupling system presents four main absorption peaks and anticrossing behavior with four branches as r_{Au} changes. Actually, they are the coupling results of four photonic quasiparticles, i.e., photon, LSP, Ex, and ENZ mode. The corresponding Hamiltonian operator that

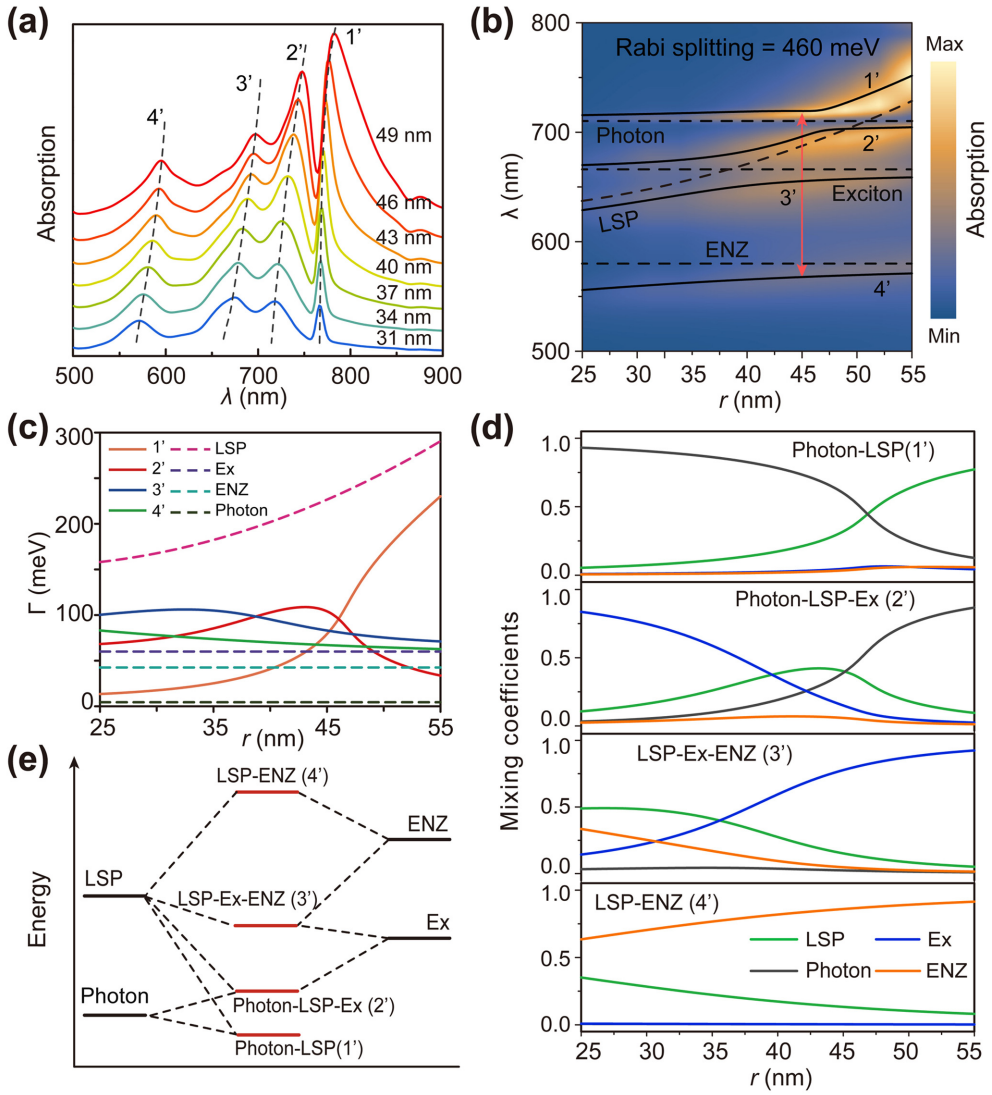

FIG. 4. (a) Absorption curves of monolayer MoS_2 coupled with a Au NA-PC cavity hybrid resonator for different values of r_{Au}. (b) Absorption spectrum of the coupled system. Dashed lines represent the uncoupled photon, LSP, Ex, and ENZ modes, respectively. The solid black line is the anticrossing curve fitted by the coupled oscillator model. (c) Linewidth as a function of r_{Au} for four uncoupled modes and four branches in (a). (d) The mixing coefficients of four uncoupled modes as function of r_{Au}. (d) Energy-state map of the coupled system.

describes such a complicated coupling process can be written as

$$\hat{\boldsymbol{H}} = \begin{pmatrix} E_{\mathrm{P}} + \frac{\mathrm{i}\hbar\Gamma_{\mathrm{P}}}{2} & g_{\mathrm{P,LSP}} & g_{\mathrm{P,Ex}} & g_{\mathrm{P,ENZ}} \\ g_{\mathrm{P,LSP}} & E_{\mathrm{LSP}} + \frac{\mathrm{i}\hbar\Gamma_{\mathrm{LSP}}}{2} & g_{\mathrm{LSP,Ex}} & g_{\mathrm{LSP,ENZ}} \\ g_{\mathrm{P,Ex}} & g_{\mathrm{LSP,Ex}} & E_{\mathrm{Ex}} + \frac{\mathrm{i}\hbar\Gamma_{\mathrm{Ex}}}{2} & g_{\mathrm{Ex,ENZ}} \\ g_{\mathrm{P,ENZ}} & g_{\mathrm{LSP,ENZ}} & g_{\mathrm{Ex,ENZ}} & E_{\mathrm{ENZ}} + \frac{\mathrm{i}\hbar\Gamma_{\mathrm{ENZ}}}{2} \end{pmatrix}, \tag{6}$$

where $E = (\boldsymbol{E}_{\mathrm{P}}, E_{\mathrm{LSP}}, E_{\mathrm{Ex}}, E_{\mathrm{ENZ}})^{\mathrm{T}}$ and $\boldsymbol{\Gamma} = (\Gamma_{\mathrm{P}}, \Gamma_{\mathrm{LSP}}, \Gamma_{\mathrm{Ex}}, \boldsymbol{\Gamma}_{\mathrm{ENZ}})^{\mathrm{T}}$ stand for the eigenenergy and linewidth of each mode, respectively. If the linewidth of each branch is defined as $\Gamma_{s\prime} = \langle s\prime|\boldsymbol{\Gamma}|s\prime\rangle$ ($s\prime$ represents $1'$, $2'$, $3'$, or $4'$), then the Rabi splitting energy of the whole system can be expressed as $\Omega = \sum_{s\prime} |\Gamma_{s\prime}|^2 / \sum_{s\prime} \Gamma_{s\prime}$. Figure 4(c) shows the linewidth of each mode or each branch as a function of r_{Au}. In particular, when r_{Au} is about 45 nm, $\hbar\Gamma_P = 4.4$ meV, $\hbar\Gamma_{\mathrm{LSP}} = 226.5$ meV, $\hbar\Gamma_{\mathrm{Ex}} = 60$ meV, and $\hbar\Gamma_{\mathrm{ENZ}} = 42.6$ meV. The linewidth of each branch is similar, i.e., $\hbar\Gamma_{1'} = 79$ meV, $\hbar\Gamma_{2'} = 104$ meV, $\hbar\Gamma_{3'} = 83$ meV, and $\hbar\Gamma_{4'} = 67$ meV. Under this condition, the whole system will enter the strongest coupling with a total Rabi splitting energy of 460 meV. The fitted coupling strengths are $g_{\mathrm{P,LSP}} = 60$ meV, $g_{\mathrm{LSP,Ex}} = 56$ meV, and $g_{\mathrm{LSP,ENZ}} = 135$ meV.

TABLE I. Comparison of strong coupling between TMDs and different plasmonic, optical, and plasmonic-optical hybrid resonators.

Structure	Two modes	$\hbar\Gamma_{\mathrm{P}}$	$\hbar\Gamma_{\mathrm{Ex}}$	$\hbar\Gamma_{\mathrm{ENZ}}$	$\hbar\Gamma_{\mathrm{LSP}}$	$\hbar\Omega_{\mathrm{R}}$
MoS_2 in FP cavity [32]	Photon/Ex	39	60			46 ± 3
MoS_2 in FP cavity [34]	Photon/Ex	14	60			54
WS_2 in FP cavity [26]	Photon/Ex	80	28			101
WS_2 in FP cavity [53]	Photon/Ex	55	34			70
Plasmonic arrays on WS_2 [26]	SPP/Ex	36	28			60
Silver nanorod on WSe_2 [54]	LSP/Ex	95	43			49.6
Gold nanorod on WS_2 [44]	LSP/Ex	149	57			133
Silver triangle on WS_2 [55]	LSP/Ex	190	20			120
Si Nanoparticle on WS_2 [56]	Magnetic dipole/Ex	84	33			116
Structure	Three modes	$\hbar\Gamma_P$	$\hbar\Gamma_{\mathrm{Ex}}$		$\hbar\Gamma_{\mathrm{LSP}}$	$\hbar\Omega_{\mathrm{R}}$
FP cavity-Ag NAs-WS_2 [38]	Photon/LSP/Ex	~142	50		320	300
Structure	Four modes	$\hbar\Gamma_P$	$\hbar\Gamma_{\mathrm{Ex}}$	$\hbar\Gamma_{\mathrm{ENZ}}$	$\hbar\Gamma_{\mathrm{LSP}}$	$\hbar\Omega_{\mathrm{R}}$
Model in this paper	Photon/LSP/Ex/ENZ	4.4	60	42.6	226.5	460

All units are meV.

The splitting energy of the whole system can be judged by the following strong-coupling criterion [38]:

$$E_{\mathrm{Rabi}} > E = W_1\hbar\Gamma_{1'} + W_2\hbar\Gamma_{2'} + W_3\hbar\Gamma_{3'} + W_4\hbar\Gamma_{4'}, \quad (7)$$

where W_1, W_2, W_3, and W_4 are the contribution weights of four branches, and they are calculated as

$$\begin{aligned} W_1 &= \Gamma_{1'}/(\Gamma_{1'} + \Gamma_{2'} + \Gamma_{3'} + \Gamma_{4'}) = 23.7\% \\ W_2 &= \Gamma_{2'}/(\Gamma_{1'} + \Gamma_{2'} + \Gamma_{3'} + \Gamma_{4'}) = 31.3\% \\ W_3 &= \Gamma_{3'}/(\Gamma_{1'} + \Gamma_{2'} + \Gamma_{3'} + \Gamma_{4'}) = 24.9\% \\ W_4 &= \Gamma_{4'}/(\Gamma_{1'} + \Gamma_{2'} + \Gamma_{3'} + \Gamma_{4'}) = 20.1\% \end{aligned} \quad (8)$$

The linewidth of each branch can be further written as

$$\Gamma_{s'} = H_{s'}^{P}\Gamma_{\mathrm{P}} + H_{s'}^{\mathrm{LSP}}\Gamma_{\mathrm{LSP}} + H_{s'}^{\mathrm{Ex}}\Gamma_{\mathrm{Ex}} + H_{s'}^{\mathrm{ENZ}}\Gamma_{\mathrm{ENZ}}, \quad (9)$$

where $H_{s'}{}^{\mathrm{P}}$, $H_{s'}{}^{\mathrm{LSP}}$, $H_{s'}{}^{\mathrm{Ex}}$, and $H_{s'}{}^{\mathrm{ENZ}}$ are the mixing (Hopfield) coefficients of photon, LSP, Ex, and ENZ mode for four branches. Based on the fitting results in Fig. 4(d), we can clearly identify the coupling modes which contribute to each branch.

For $r_{\mathrm{Au}} = 45$ nm, the strong-coupling criteria related to the four uncoupled modes can be calculated as $E = 27.04\%\hbar\Gamma_P + 26.56\%\hbar\Gamma_{\mathrm{LSP}} + 25.24\%\hbar\Gamma_{\mathrm{Ex}} + 21.16\%\hbar\Gamma_{\mathrm{ENZ}} = 85.5$ meV. Consequently, the total Rabi splitting energy of our proposed composite structure ($E_{\mathrm{Rabi}} = 460$ meV) is much higher than the strong-coupling criterion (85.5 meV) and is also superior to the Rabi splitting energy of monolayer MoS_2 coupled with single Au NA ($E_{\mathrm{Rabi}} = 375$ meV), which demonstrates that the introduction of a PC cavity can efficiently enhance the strong coupling between monolayer MoS_2 and Au NA. The complicated coupling process of four photonic quasiparticles in our proposed composite structure can be described by the energy-state map as shown in Fig. 4(e).

Table I compares the strong-coupling model proposed in this paper with previous models related to TMD materials coupled with different plasmonic or optical resonators. Our model, which extends the number of photonic quasiparticles from two or three to four, shows the largest Rabi splitting energy. Except for MoS_2, other TMD materials such as WS_2 and WSe_2 are also suitable for the strong-coupling study based on our proposed plasmonic-optical resonator. Although the plasmonic resonator used here is related to the LSP, other plasmonic resonators which support the surface plasmon polariton (SPP), such as the subwavelength plasmonic array and graphene waveguides [26,57–59], are expected to be designed to explore the strong-coupling phenomena and underlying mechanism in the TMDs coupled with the SPP-PC cavity hybrid system. Moreover, although the spin of exciton is not considered in the current work, the exciton polaritons which possess the distinctive spin-polarization degree of freedom in the TMDs are expected to be studied for potential application in the optical spin Hall effect based on our proposed model [60,61].

Conclusion. In this paper we have demonstrated a large Rabi splitting of up to 460 meV in monolayer MoS_2 coupled with a Au NA-PC cavity hybrid resonator. We have clearly revealed the formation mechanisms of each branch and calculated the contribution weights of photon, LSP, Ex, and ENZ mode on each branch. The results of this work will provide useful reference for other groups to study the strong light–matter interactions with multiple photonic quasiparticles in TMD materials coupled with different plasmonic-optical hybrid resonators.

Acknowledgments. This work was supported in part by the National Natural Science Foundation of China (NSFC) (Grants No. 61675096 and No. 61205042), Six Talent Climax Foundation of Jiangsu (Grant No. XYDXX-027), Fundamental Research Funds for the Central Universities (Grant No. 30919011106), and the Open Research Fund of State Key Laboratory of Bioelectronics (Grant No. Sk1b2021p06). In addition, the authors acknowledge support from the Ministry of Education of Singapore for the funding of this research through AcRF Tier 1 grants (Grants No. RG103/16 and No. RG195/17) and a Tier 3 grant (Grant No. MOE2016-T3-1-006 (S)).

[1] M. Waldherr, N. Lundt, M. Klaas, S. Betzold, M. Wurdack, V. Baumann, E. Estrecho, A. Nalitov, E. Cherotchenko, H. Cai, E. A. Ostrovskaya, A. V. Kavokin, S. Tongay, S. Klembt, S. Höfling, and C. Schneider, Nat. Commun. **9**, 3286 (2018).

[2] L. Novotny, Am. J. Phys. **78**, 1199 (2010).

[3] W. Guerin, T. S. do Espirito Santo, P. Weiss, A. Cipris, J. Schachenmayer, R. Kaiser, and R. Bachelard, Phys. Rev. Lett. **123**, 243401 (2019).

[4] F. J. Garcia-Vidal and J. Feist, Science **357**, 1357 (2017).

[5] P. Vasa, W. Wang, R. Pomraenke, M. Maiuri, C. Manzoni, G. Cerullo, and C. Lienau, Phys. Rev. Lett. **114**, 036802 (2015).

[6] R. Chikkaraddy, B. de Nijs, F. Benz, S. J. Barrow, O. A. Scherman, E. Rosta, A. Demetriadou, P. Fox, O. Hess, and J. J. Baumberg, Nature (London) **535**, 127 (2016).

[7] A. I. Vakevainen, R. J. Moerland, H. T. Rekola, A. P. Eskelinen, J. P. Martikainen, D. H. Kim, and P. Torma, Nano Lett. **14**, 1721 (2014).

[8] H. Gross, J. M. Hamm, T. Tufarelli, O. Hess, and B. Hecht, Sci. Adv. **4**, eaar4906 (2018).

[9] K. Santhosh, O. Bitton, L. Chuntonov, and G. Haran, Nat. Commun. **7**, 11823 (2016).

[10] J. Qin, Y.-H. Chen, Z. Zhang, Y. Zhang, R. J. Blaikie, B. Ding, and M. Qiu, Phys. Rev. Lett. **124**, 063902 (2020).

[11] C. Schneider, M. M. Glazov, T. Korn, S. Höfling, and B. Urbaszek, Nat. Commun. **9**, 2695 (2018).

[12] L. Sun, Z. Li, J. He, and P. Wang, Nanophotonics **8**, 1835 (2019).

[13] K. F. Mak, C. Lee, J. Hone, J. Shan, and T. F. Heinz, Phys. Rev. Lett. **105**, 136805 (2010).

[14] D. Xiao, G.-B. Liu, W. Feng, X. Xu, and W. Yao, Phys. Rev. Lett. **108**, 196802 (2012).

[15] L. F. Sun, J. X. Yan, D. Zhan, L. Liu, H. L. Hu, H. Li, B. K. Tay, J. L. Kuo, C. C. Huang, D. W. Hewak, P. S. Lee, and Z. X. Shen, Phys. Rev. Lett. **111**, 126801 (2013).

[16] X. Qian, J. Liu, L. Fu, and J. Li, Science **346**, 1344 (2014).

[17] S. Bhattacharyya and A. K. Singh, Phys. Rev. B. **86**, 075454 (2012).

[18] J. Xia, J. X. Yan, Z. H. Wang, Y. M. He, Y. J. Gong, W. Q. Chen, T. C. Sum, Z. Liu, P. M. Ajayan, and Z. X. Shen, Nat. Phys. **17**, 92 (2021).

[19] H. Shan, Y. Yu, X. Wang, Y. Luo, S. Zu, B. Du, T. Han, B. Li, Y. Li, J. Wu, F. Lin, K. Shi, and B. K. Tay, Z. Liu, Light-Sci. Appl. **8**, 9 (2019).

[20] P. Sriram, A. Manikandan, F.-C. Chuang, and Y.-L. Chueh, Small **16**, 1904271 (2020).

[21] X. Wen, W. Xu, W. Zhao, J. B. Khurgin, and Q. Xiong, Nano Lett **18**, 1686 (2018).

[22] Y. Kang, S. Najmaei, Z. Liu, Y. Bao, Y. Wang, X. Zhu, N. J. Halas, P. Nordlander, P. M. Ajayan, J. Lou, and Z. Fang, Adv. Mater. **26**, 6467 (2014).

[23] J. Sun, Y. Li, H. Hu, W. Chen, D. Zheng, S. Zhang, and H. Xu, Nanoscale **13**, 4408 (2021).

[24] W. Du, J. Zhao, W. Zhao, S. Zhang, H. Xu, and Q. Xiong, ACS Photonics **6**, 2832 (2019).

[25] Y. Yu, Z. Ji, S. Zu, B. Du, Y. Kang, Z. Li, Z. Zhou, K. Shi, and Z. Fang, Adv. Funct. Mater. **26**, 6394 (2016).

[26] S. Wang, S. Li, T. Chervy, A. Shalabney, S. Azzini, E. Orgiu, J. A. Hutchison, C. Genet, P. Samorì, and T. W. Ebbesen, Nano Lett. **16**, 4368 (2016).

[27] X. Liu, W. Bao, Q. Li, C. Ropp, Y. Wang, and X. Zhang, Phys. Rev. Lett. **119**, 027403 (2017).

[28] Y. Tang, Y. Zhang, H. Ouyang, M. Zhao, H. Hao, K. Wei, H. Li, Y. Sui, J. You, X. Zheng, Z. Xu, X. Cheng, L. Shi, and T. Jiang, Laser Photonics Rev. **14**, 1900419 (2020).

[29] T. Yoshie, A. Scherer, J. Hendrickson, G. Khitrova, H. M. Gibbs, G. Rupper, C. Ell, O. B. Shchekin, and D. G. Deppe, Nature (London) **432**, 200 (2004).

[30] Y. Mi, Z. Zhang, L. Zhao, S. Zhang, J. Chen, Q. Ji, J. Shi, X. Zhou, R. Wang, J. Shi, W. Du, Z. Wu, X. Qiu, Q. Zhang, Y. Zhang, and X. Liu, Small **13**, 1701694 (2017).

[31] M. Roiz, A. Monakhov, E. Kunitsyna, Y. Yakovlev, R. Teissier, and A. Baranov, J. Appl. Phys. **127**, 173105 (2020).

[32] X. Liu, T. Galfsky, Z. Sun, F. Xia, E.-c. Lin, Y.-H. Lee, S. Kéna-Cohen, and V. M. Menon, Nat. Photonics **9**, 30 (2015).

[33] T. Galfsky, Z. Sun, C. R. Considine, C.-T. Chou, W.-C. Ko, Y.-H. Lee, E. E. Narimanov, and V. M. Menon, Nano Lett. **16**, 4940 (2016).

[34] T. Hu, Y. Wang, L. Wu, L. Zhang, Y. Shan, J. Lu, J. Wang, S. Luo, Z. Zhang, L. Liao, S. Wu, X. Shen, and Z. Chen, Appl. Phys. Lett. **110**, 051101 (2017).

[35] N. Lundt, S. Klembt, E. Cherotchenko, Betzold S, O. Iff, A. V. Nalitov, M. Klaas, C. P. Dietrich, A. V. Kavokin, S. Höfling, and C. Schneider, Nat. Commun. **7**, 13328 (2016).

[36] L. Shi, T. K. Hakala, H. T. Rekola, J. P. Martikainen, R. J. Moerland, and P. Törmä, Phys. Rev. Lett. **112**, 153002 (2014).

[37] A. Tsargorodska, M. L. Cartron, C. Vasilev, G. Kodali, O. A. Mass, J. J. Baumberg, P. L. Dutton, C. N. Hunter, P. Törmä, and G. J. Leggett, Nano Lett. **16**, 6850 (2016).

[38] B. Li, S. Zu, Z. Zhang, L. Zheng, Q. Jiang, B. Du, Y. Luo, Y. Gong, Y. Zhang, F. Lin, B. Shen, X. Zhu, P. M. Ajayan, and Z. Fang, Opto-Electron. Adv. **2**, 190008 (2019).

[39] Y. Akahane, T. Asano, B. S. Song, and S. Noda, Nature (London) **425**, 944 (2003).

[40] Y. S. Peng, M. H. Yao, R. C. Li, and Z. G. Wang, Opt. Commun. **285**, 1510 (2012).

[41] P. B. Johnson and R. W. Christy, Phys. Rev. B. **6**, 4370 (1972).

[42] Y. Li, A. Chernikov, X. Zhang, A. Rigosi, H. M. Hill, A. M. van der Zande, D. A. Chenet, E. M. Shih, J. Hone, and T. F. Heinz, Phys. Rev. B. **90**, 205422 (2014).

[43] D. Y. Qiu, F. H. da Jornada, and S. G. Louie, Phys. Rev. Lett. **111**, 216805 (2013).

[44] J. Wen, H. Wang, W. Wang, Z. Deng, C. Zhuang, Y. Zhang, F. Liu, J. She, J. Chen, H. Chen, S. Deng, and N. Xu, Nano Lett. **17**, 4689 (2017).

[45] A. M. Khasraghi, S. Shojaei, A. S. Vala, and M. Kalafi, Physica E **47**, 17 (2013).

[46] M. A. K. Othman, C. Guclu, and F. Capolino, Opt. Express **21**, 7614 (2013).

[47] X. Niu, X. Hu, S. Chu, and Q. Gong, Adv. Opt. Mater. **6**, 1701292 (2018).

[48] Y. S. Joe, A. M. Satanin, and C. S. Kim, Phys. Scripta **74**, 259 (2006).

[49] M. F. Limonov, M. V. Rybin, A. N. Poddubny, and Y. S. Kivshar, Nat. Photonics **11**, 543 (2017).

[50] A. A. Dmitriev and M. V. Rybin, Phys. Rev. A. **99**, 063837 (2019).

[51] B. Peng, S. K. Özdemir, W. Chen, F. Nori, and L. Yang, Nat. Commun. **5**, 5082 (2014).

[52] See Supplemental Material at http://link.aps.org/supplemental/10.1103/PhysRevB.104.205118 for more results and discussion on the coupling between Au NA and the PC cavity as well as the coupling between the PC cavity and monolayer.

[53] L. C. Flatten, Z. He, D. M. Coles, A. A. P. Trichet, A. W. Powell, R. A. Taylor, J. H. Warner, and J. M. Smith, Sci. Rep. **6**, 33134 (2016).

[54] D. Zheng, S. Zhang, Q. Deng, M. Kang, P. Nordlander, and H. Xu, Nano Lett. **17**, 3809 (2017).

[55] J. Cuadra, D. G. Baranov, M. Wersall, R. Verre, T. J. Antosiewicz, and T. Shegai, Nano Lett **18**, 1777 (2018).

[56] S. Lepeshov, M. Wang, A. Krasnok, O. Kotov, T. Zhang, H. Liu, T. Jiang, B. Korgel, M. Terrones, Y. Zheng, and A. Alú, Acs Appl. Mater. Inter. **10**, 16690 (2018).

[57] E. H. Hwang and S. Das Sarma, Phys. Rev. B. **75**, 205418 (2007).

[58] D. Dahal, G. Gumbs, and D. Huang, Phys. Rev. B. **98**, 045427 (2018).

[59] O. L. Berman, G. Gumbs, and Y. E. Lozovik, Phys. Rev. B. **78**, 085401 (2008).

[60] O. L. Berman, R. Y. Kezerashvili, and Y. E. Lozovik, Phys. Rev. B. **99**, 085438 (2019).

[61] M. I. Vasilevskiy, D. G. Santiago-Perez, C. Trallero-Giner, N. M. R. Peres, and A. Kavokin, Phys. Rev. B. **92**, 245435 (2015).